Channeling and stress during fluid and suspension flow in self-affine fractures

Tak Shing Lo and Joel Koplik

Benjamin Levich Institute and Department of Physics, City College of the City University of New York, New York, New York 10031, USA

(Received 18 September 2013; published 13 February 2014)

The flow of fluids and particulate suspensions in realistic models of geological fractures is investigated by lattice Boltzmann numerical simulations. The walls are synthetic self-affine fractal surfaces combined to produce a tight fracture, the fluid is a viscous Newtonian liquid, and the particles are rigid noncolloidal solid spheres. One focus is channeling phenomena, where we compare the fracture aperture, the preferred paths for fluid flow, and the preferred paths for suspended particles. The preferred paths are found to be somewhat similar for pure fluid and particulates and not immediately related to the fracture aperture map. We further investigate the (tensor) stress exerted on the fracture walls. Wall roughness tends to decrease stress by reducing the flow velocities adjacent to it, an effect enhanced by the presence of particulates. Last, we examine the stress probability distributions and their spatial correlation functions.

DOI: 10.1103/PhysRevE.89.023010 PACS number(s): 47.57.E−, 47.55.Kf, 47.56.+r, 47.11.Qr

I. INTRODUCTION

Flow through rock fractures is a key ingredient in fluid recovery from aquifers and hydrocarbon reservoirs [1–3] and many other applications and displays some unusual characteristics originating in the special features of fracture geometry. Very often the flowing fluids are not clean. They are mixed with solid particles that either exist naturally or are added artificially by intention. For example, in the process of hydraulic fracturing (or fracking) for oil and natural gas recovery, a fluid is pumped under high pressure into a rock formation to create or restore small fractures in order to stimulate production from new and existing oil and gas wells. The fracking fluid is mainly a mixture of water and sand or other ceramic materials (with some other chemicals). Fracking enables the recovery of oil and natural gas from formations that geologists once believed to be impossible to produce, such as tight shale formations, and extends the production lifetime of oil and gas fields. In geothermic applications, water is injected into the fracture networks of a geothermal system to extract the heat underground. The heat exchange rate clearly depends on the flow field in the fractures and usually the underground water is not clear. The transport of fluids and dissolved or suspended contaminants in fractured rocks is also of great interest for practical applications such as soil or water pollution and waste storage.

At first glance a fracture may be approximated as a slablike pore space, and modeling based on this approximation provides a simple description of fluid flow. In this approximation, the simple "cubic law" [4] would account for Newtonian fluid flow and sediment transport would be treated with no additional complications in the same manner as well-studied suspension flow in a flat channel. In fact, fracture walls are rough and this roughness complicates the description of fluid transport and introduces trapping phenomena into sediment transport. The roughness in many cases is not random but that of a self-affine fractal surface [5,6], which induces corrections to the cubic law and long-ranged correlations in dispersion processes, among other effects. For wide fractures, the cubic law may be preserved in a usable manner by introducing a roughness correction factor [7], but in the case of tight fractures, the geometry is qualitatively altered. In this case, a further consequence of roughness is flow channeling [8], leading to reduced transport efficiency and anisotropy in permeability. Fluid flow tends to concentrate along the widest flow paths spanning the fracture, which are only a subset of the void space and need not align locally along the pressure gradient or average flow directions. Particle motion requires a channel aperture larger than the particle diameter, which renders some regions of a tight fracture interior inaccessible [9], and, furthermore, particles are carried along with the channeled flowing fluid at least in part, so "particle channeling" is an inevitable result. Furthermore, a tight channel acts in some respects as a size-selective filter and the accumulation of particles further reduces permeability while fostering anisotropy [10,11]. The result is that a particle-laden fluid moving through a fracture has an extremely inhomogeneous and time-dependent character, involving slow and fast regions of fluid flow and empty, pinned, slow and fast regions of particle flow. Furthermore, as we shall see below, the fast regions for fluid and particles coincide only partially. These variations in velocity are accompanied by variations in stress, which in addition to hydrodynamic effects leads to inhomogeneity in the stress exerted on the fracture walls.

In this paper we present unified numerical simulations of fluid and particulate suspension flow in narrow self-affine fractures in order to study the effects of this particular tortuous geometry on transport. The calculations employ the lattice Boltzmann (LB) method [12], which is ideally suited for the irregular geometry of a fracture. As a by-product of the flow calculations, the local tensor stress field within the fracture is available and we report on the stress that flowing fluid and particulate suspensions exert on the fracture walls. In previous work we have applied the same methodology to the study of permeability [13], dispersion [14], anisotropy [15], and non-Newtonian effects [16] in simple fluid flow and in particular on flow and sedimentation [17,18]. The latter paper considers the situation complementary to this paper—transport of concentrated and homogeneously distributed noncolloidal suspensions in model fractures with self-affine surfaces but whose minimum aperture exceeds several particle diameters and which are everywhere open to particle transport.

II. NUMERICAL METHOD

Our computations are based on the single-relaxation time formulation of the lattice Boltzmann method [12] in which artificial fluid particles move according to a discretized Boltzmann equation on a highly connected three-dimensional lattice. The solid particles are represented by a set of adjacent nodes within a certain radius of a center for a spherical particle, which translate and rotate according to the Newton and Euler equations in response to the net force and torque exerted by the neighboring fluid nodes [19,20]. Though we have spherical particles in mind, the particles represented in this way essentially have rough boundaries and are not perfect spheres under this numerical approximation. The solid boundaries are modeled by nodes containing neither solid nor fluid, and the no-slip condition is enforced there by the "bounce-back" rule. An explicit short-distance repulsive lubrication force between particles is added to prevent accidental overlap due to numerical inadequacy [21,22]. Further details on the implementation and numerical tests of the method are given in Ref. [23].

We consider pressure-driven flow and gravitational sedimentation of a noncolloidal particulate suspension flowing through a 3D fracture channel bounded by two complimentary surfaces. The two bounding surfaces are separated by some distance in the direction normal to the mean plane and the top (upper) surface is shifted relative to the bottom (lower) one by a shear displacement $\mathbf{R}$ in the lateral direction. Experimental investigations show that natural fracture surfaces are self-affine and the surface height $z(x,y)$ exhibits a power-law correlation,

$$C(r) = \langle [z(\mathbf{r}+\mathbf{r}_0) - z(\mathbf{r}_0)]^2 \rangle \sim r^{2H}. \quad (1)$$

Here $r = |\mathbf{r}|$ ($\mathbf{r}$ is a vector on the base plane) and H is known as the Hurst exponent. The Hurst exponent is a material constant which depends on the type of rock considered [6]. We adopt the value $H = 0.8$, which is appropriate for granite, for consistency with our previous work on fracture flow [13–15,18], and the surface is generated statistically by a Fourier synthesis method [24]. The roughness of the surface is controlled by the variance σ^2 of the surface height, and the generated surface is rescaled so the standard deviation $\sigma = 10$ lattice spacings which is the size of the particles. The gap between the top and the bottom surfaces is the aperture of the channel and the aperture field $h(x,y)$ varies from place to place if $\mathbf{R} \neq 0$. We take x as the mean flow direction along which a pressure gradient G is applied, y is the neutral or vorticity direction, and a gravitational acceleration of strength g is applied in the downward z direction. The flow domain is a simulation box of dimensions $L_x \times L_y \times L_z$ and periodic boundary conditions are applied both in the x and y directions. We consider the general case in which the shear displacement $\mathbf{R}$ does not align with the x nor the y directions. The geometry of the channel used in the simulations is sketched in Fig. 1(a). In Fig. 1(b), the surface height profile of the bottom surface used to construct our fracture channel is shown.

We assume that the suspending fluid is Newtonian and the suspended particles have a density ρ_s greater than or equal to the density of the fluid ρ, which is typical in natural geological processes that involve minerals suspended in water. We assume that the suspension is monodisperse and the particles are

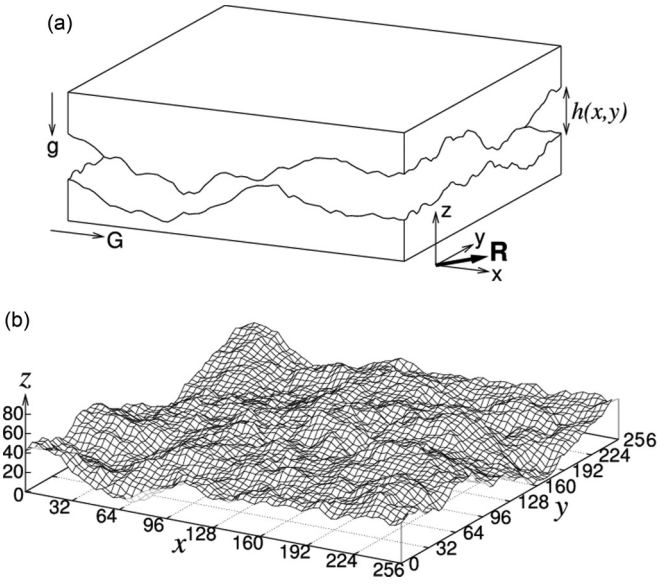

FIG. 1. (a) Schematic drawing of the fracture channel used in the simulations. The two bounding surfaces are complimentary and self-affine. The upper (top) surface is displaced vertically upward and shifted laterally by a displacement $\mathbf{R}$ relative to the lower (bottom) surface, generating an aperture $h(x,y)$ in between. (b) Height profile of the bottom surface used to generate the fracture channel used in the simulations.

spheres with diameter $d = 10$ lattice spacings. The size of the simulation box is $L_x = L_y = 25.6d$. The height profile $h_2(\mathbf{r})$ of the upper surface is related to the profile $h_1(\mathbf{r})$ of the lower one by $h_2(\mathbf{r}) = h_1(\mathbf{r}-\mathbf{R}) + s$ (see Fig. 1), where s the shift in the vertical (z) direction. We use $\mathbf{R} = 10\mathbf{i} + 10\mathbf{j}$ and $s = 27$ lattice spacings. The precise values of these two choices are somehow arbitrary, except that $|\mathbf{R}|$ is large compared the lattice spacing and small compared to the lateral dimensions of the channel, both $|\mathbf{R}|$ and s are comparable to the size of the particles, and the resulting aperture field looks realistic. As a result, the channel width L_z is $9.3d$ and the mean aperture of the channel, as obtained by dividing the total free space volume in the gap by the base plane area, is $2.7d$. Contour maps of the aperture fields of the fracture channels used in the simulations are shown in Fig. 2.

The global particle concentration in the channel is controlled by the number of particles, N_p, placed in the domain. Simulations are performed at $N_p = 81$, 163, 244, 325, and 407, giving a range in the bulk solid volume fraction ϕ from 0.025 to 0.125 based on the free volume in the gap. These nominal particle concentrations seem to be dilute. However, consider the fact that much of the space is inaccesible to the particles but still allows fluid to flow, due to the geometry of the rough surfaces: The suspension is actually quite dense in the high end of N_p. Clearly, a more reasonable measure of the particle concentration that takes the "dead" space of the channel into account must essentially be geometry dependent. In the absence of a better way to define the concentration due to the complicated geometry, we shall stick to this nominal concentration. In addition, we also simulate a pressure-driven flow of pure fluid through the same channel with no particle, i.e., $\phi = 0$, and the results provide a basis for comparison.

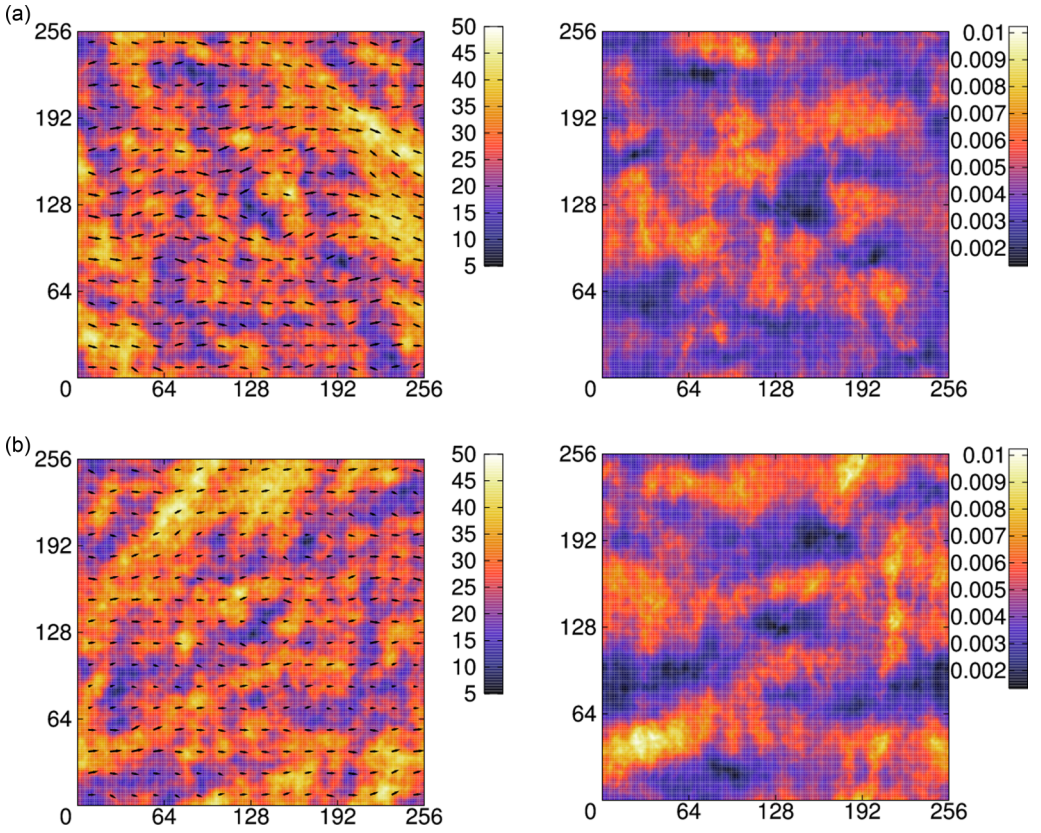

FIG. 2. (Color online) (a) The aperture field (left) of the fracture channel used in the simulations and the steady-state gap-averaged 2D fluid speed (right) for a pressure-driven flow of pure fluid without particle through the channel. The vectors on top of the aperture field indicate the gap-averaged 2D fluid velocity field. (b) The same plots as in (a) except that the channel is rotated 90° counterclockwise.

At the start of the simulations, the particles are uniformly distributed inside the channel without overlapping with the walls and all particles and the fluid are set at rest. We focus on steady-state results in this paper. The numerical computations are performed in dimensionless "lattice Boltzmann units," where the lattice spacing a and the time step τ are both unity, there is unit mass at each node, the pressure gradient G is imposed as a (dimensionless) body force, and the relaxation time in the Boltzmann equation is 0.8 corresponding to a kinematic viscosity $\nu = 0.1$. In this work, we use $G = 2 \times 10^{-5}$ and $g = 0.001$. To have a feeling for the scales involved in a physical realization, consider $d = 100\ \mu$m diameter particles which when resolved with 10 lattice units corresponds to lattice spacing $a = 10\ \mu$m. If we interpret the kinematic viscosity as a vorticity diffusion time, $\nu = a^2/(6\tau)$, and choose water as the pore fluid, then the time step is $\tau \approx 17\ \mu$s. Since typical dimensionless average fluid velocities turn out to be $O(10^{-3})$, the physical fluid velocities are 0.01–0.1 cm/s.

III. RESULTS

A. Simulations of pure fluid flows

First we present the geometry and characterizations of the fracture channel used in the simulations and the steady-state results of a pressure-driven flow of a pure fluid through the channel. In Fig. 2, the contour map of the aperture field of the channel is shown on the left side of the figure. Two simulations were performed, the one in Fig. 2(a) (top row) and one with the channel rotated 90° counterclockwise relative to the first one, as shown in Fig. 2(b) (bottom). In both cases, the pressure drops are applied in the positive x direction in the figure. As can be seen from the figure, the local aperture has a broad distribution about the mean $2.7d$. However, due to the fact that the particles have a finite diameter $d = 10$ lattice spacings, actually a lot of the space in the channel is inaccessible to the particles. The distribution of the local aperture field is shown quantitatively in Fig. 3.

In Fig. 4, the surface height correlation functions of the two bounding surfaces used to create the channel is shown. We also computed the correlation function of the aperture field according to the same definition as in Eq. (1) and plotted it in the same figure. Since the two bounding surfaces are complementary, the correlations in the heights of the top and the bottom are identical. Even though we generated a self-affine surface with Hurst exponent $H = 0.8$, the correlation in surface height in this case scales as $r^{1.45}$ instead of $r^{1.6}$. Presumably, the discrepancy is due to truncation of the generated surface to integer height in order to fit in the lattice of the lattice Boltzmann scheme. In this case, the aperture field has roughly the same power-law correlation as the bounding surfaces, but the correlation extends only to a range of about 10 lattice spacings (size of the particle), which is consistent with the fact that spatial correlations in the aperture field decay over a characteristic length of the order of the shear displacement **R** [25].

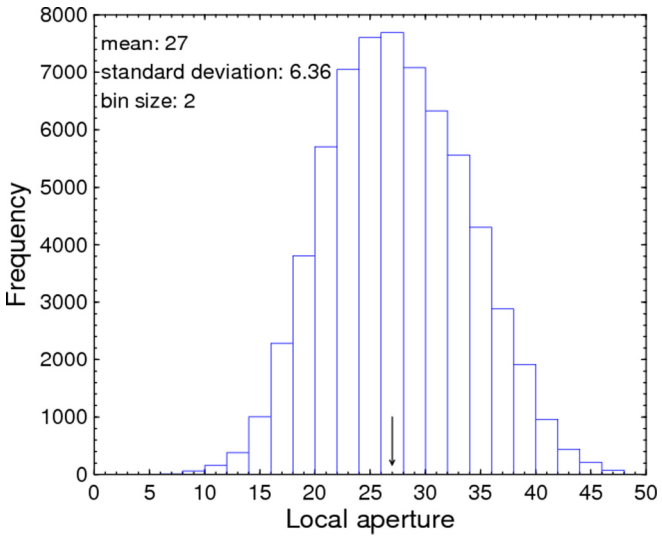

FIG. 3. (Color online) Distribution of the local aperture of the fracture channel used in the simulations. The arrow marks the average aperture.

In order to visualize the flow pattern inside the channel, we consider the gap-averaged fluid velocity field obtained by averaging the 3D fluid velocities over the gap of the fracture at each point (x,y) on the base plane. The result is a representation of the 3D velocity field defined on a 2D plane. Since the average aperture $(2.7d)$ is small compared to the lateral size of the channel $(25.6d)$ and for most of the time we are only interested in the motion in the lateral directions, this representation is reasonable and convenient. Later we shall similarly define a gap-averaged particle velocity field when we analyze the simulations with particles. On the left of Fig. 2, the gap-averaged 2D velocity field (i.e., only the x and y components) of a flow without particles is plotted as a vector field on top of the aperture, showing the slight deviation of the flow from the mean flow direction. The steady-state average flow velocity of the channel in Fig. 2(a) in the mean flow direction is 4.296×10^{-3}, while for the rotated channel in Fig. 2(b), the average flow velocity is slightly higher and is 4.741×10^{-3} in this case. For references, the average flow speed for the Poiseuille flow of the same fluid at the same pressure drop in a flat channel of width equal to the mean aperture of our fracture channel is 1.127×10^{-2}. The additional resistance due to surface roughness and the fluctuations in aperture results in roughly 2.5 times reduction in the mean flow rate in this case. On the right of Fig. 2, we plot the speed of the gap-averaged 2D velocity field (i.e., motion in the z direction is ignored). It shows that the fast flow regions tend to form elongated channels along the mean flow direction [8].

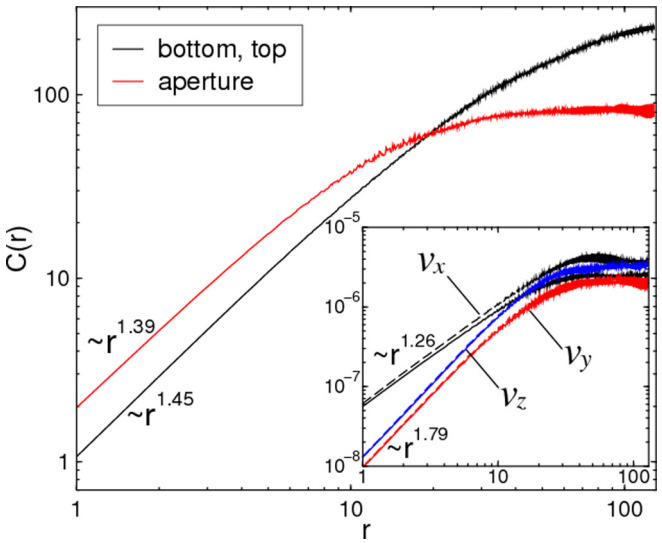

FIG. 4. (Color online) Correlation functions of the self-affine surface used to construct the channel and the aperture field of the channel. The inset shows the correlations of the gap-averaged steady-state fluid velocity field of pressure-driven flows of a pure fluid through the channel in Fig. 2(a) (solid line) and the rotated channel in Fig. 2(b) (dashed line).

It is known that spatial correlations in fracture surfaces can produce observable effects in, for example, the dispersion front of a passive tracer [14], presumably via correlations in the fluid velocity. However, the actual correlations in the flow velocity field have never been demonstrated before. To understand more the effects of the fracture geometry on the flow field, we analyze the spatial correlations in the gap-averaged velocity field according to Eq. (1) and the results are shown in the inset of Fig. 4. It is clear that all three components of the gap-averaged velocity field are spatially correlated. The correlation functions obey a power law in a range similar to that in the aperture field. In the neutral (v_y) and the vertical (v_z) directions, the correlation functions have the same exponent, 1.79, which is close to 1.6, as expected from $H = 0.8$. On the other hand, the power-law exponent is smaller and is equal to 1.26 for the correlations in the mean flow component (v_x). If the correlations in the speed is considered instead of the individual components of the gap-averaged velocity field, the correlation function will be dominated by the one for v_x since this is the one with the largest magnitude.

In additional to the flow field, one is also concerned with the forces and stresses acting on the bounding rock surfaces when a fluid or a particle suspension flows through a fracture since they determine the mechanical responses of the solid. In general, stresses are difficult to compute for flows through irregular geometry. But with the lattice Boltzmann method, the shear stress tensor $\sigma_{ij} = \mu(\partial_i u_j + \partial_j u_i)$ in the fluid can be determined easily on the fly during the simulations [26]. We obtain the total stress $-P\delta_{ij}+\sigma_{ij}$, where P is the local pressure, at the fluid sites next to the solid surfaces of the channel and from this, we calculate the local stresses and forces acting on the two bounding surfaces. We shall focus on the normal force $F_z = -P + \sigma_{zz}$ in the z direction, the usual shear stress given by σ_{zx}, and the normal force acting in the x direction given by $F_x = -P + \sigma_{xx}$. The last component is the force acting on a wall in the x direction due to the flow in the same direction. It is interesting because this force vanishes for a flat channel. But for a channel with rough walls, the fluctuations in the height profile obstruct the flow and result in this additional force component. The (2D) distribution of the normal stress force F_z, the shear stress force, and the normal stress force F_x acting on the two solid walls for a pure fluid

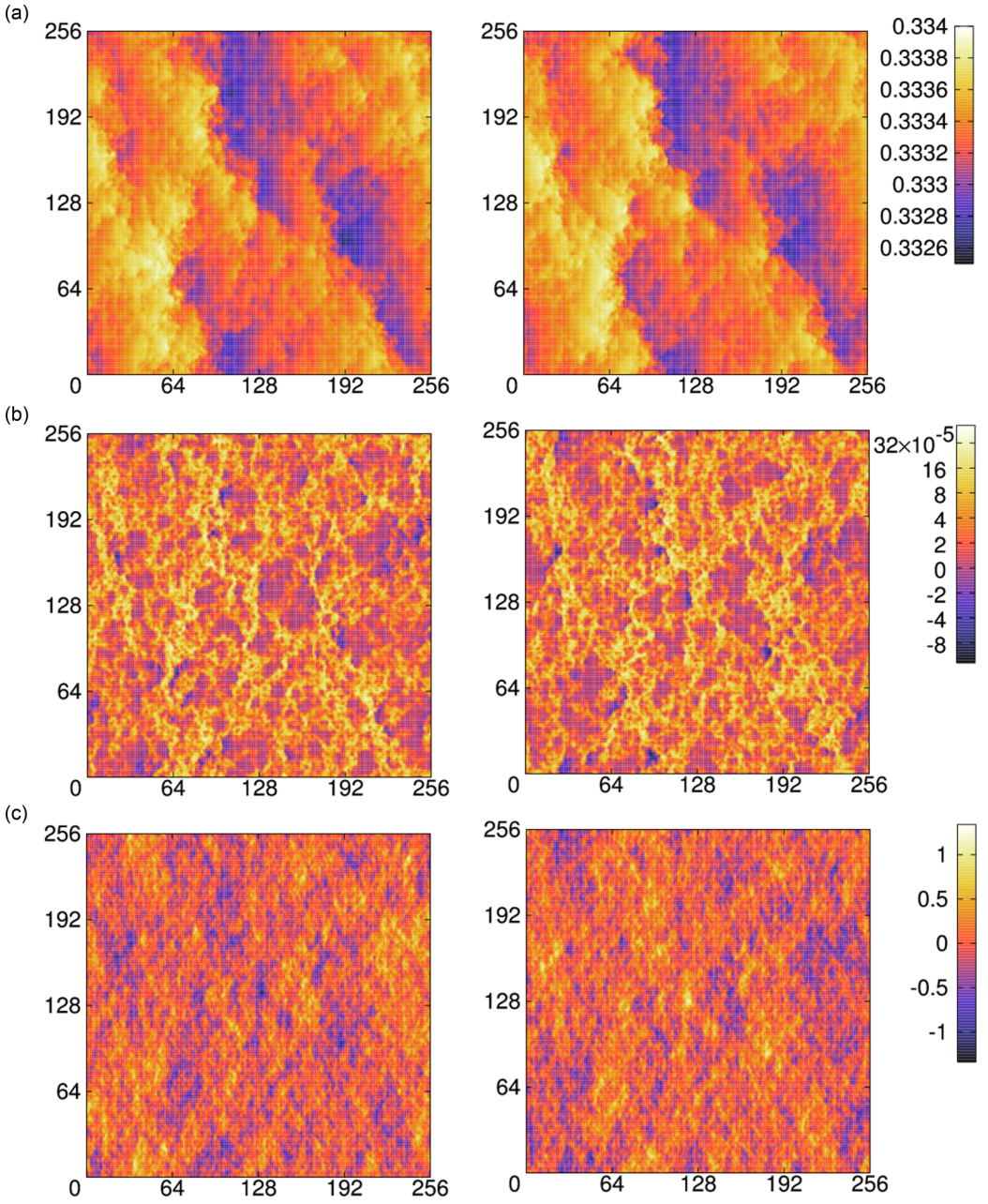

FIG. 5. (Color online) (a) The local normal force F_z in the z direction, (b) local shear stress force in the x direction, and (c) local normal force F_x in the x direction acting on the two bounding surfaces for the pressure-driven flow of a pure fluid through the channel in Fig. 2(a). The column on the left is for the top surface and the one on the right is for the bottom. The normal force F_z on the bottom is actually acting downward and is negative, but only the magnitude of F_z is shown here.

flowing through the fracture channel in Fig. 2(a) are shown in Fig. 5. These are the local stresses on the walls shown as a 2D map, that is, we add all the contributions of the stresses at different heights on the walls at each base point (x, y) and plot the sum on the xy plane with a color scale. The stresses acting on the bounding surfaces of the rotated channel in Fig. 2(b) are qualitatively similar. For the normal stress force F_z in Fig. 5(a), the force on the bottom surface (as shown on the right) is actually acting downward and should be negative, but only the magnitude of the force is shown here. Figure 5(a) shows that the normal stress force F_z in the vertical direction is dominated by the hydrostatic pressure and only varies slightly around $1/3$—the value for Poiseuille flow in a flat channel. However, the forces on the top and the bottom surfaces are highly correlated (except that they should have opposite signs). The distribution of the shear stress forces on the top and bottom surfaces of the channel are shown on the left and the right of Fig. 5(b), respectively. Naturally, the distribution of the shear stress is inhomogeneous as expected due to the nonuniformity of the fracture surface. The interesting point here is that there are local regions where the shear stress is negative even though the fluid flow is always in the mean flow direction. The average steady-state shear stresses are 4.478×10^{-5} for the top and 4.496×10^{-5} for the bottom. This is approximately 6 times

smaller than the shear stress at the walls of an equivalent flat channel of width equal to the mean aperture subject to the same pressure gradient. The reduction is presumably due to the reduced flow rate as a result of the addition resistance from the rough surfaces. But note that the shear stress on the rough surfaces has a large fluctuation about the mean value and the maximum is about 4 times higher than the stress of the equivalent flat channel. Finally, the local normal stress force F_x in the x direction at the top and bottom of the channel are shown in Fig. 5(c). This component would be zero for a flat channel because this is the force acting on the vertical parts of the channel walls. In this case, the average steady-state value is 1.453×10^{-4} for the top and 1.342×10^{-4} for the bottom, with a large fluctuation. A closer look into the distribution indicates that F_x is actually dominated by the hydrostatic pressure, but the forward-facing vertical area of the walls is the same as the backward-facing one, the total force sums up and averages out to give a small average value. Nevertheless, the magnitude is consistent with the order of magnitude of the shear stress and its sign indicates that the mean flow is in the positive x direction.

We analyzed the distributions of the shear stress force and the normal stress force F_z in the vertical direction quantitatively for the two channels in Fig. 2 and plot the logarithm of the probability distributions versus the stress forces in Fig. 6. The forces are standardized by subtracting the mean from the force and then dividing by the standard deviation. We found that, after the standardization, the two stress components acting on the two walls for the two different channels collapse into two different master curves even though the forces on the two surfaces and for flows in different orientations have different means and standard deviations. However, the behaviors for the two normalized curves differ substanitally. For the shear stress force, the semilog plot of the probability distribution versus the stress as shown in Fig. 6(a) fall on two straight lines on both sides about a maximum point close to the mean, showing that the distribution of the shear stress is exponential. More interestingly, the decay rates of the distributions differ for shear stresses above and below the mean value. We also performed additional simulations of a pure fluid flowing through two other channels constructed from shifted complimentary surfaces of completely different geometry, each one for flows in two different orthogonal directions, and found that the normalized shear stress data also collapse to the same two curves in Fig. 6(a). So this behavior in the shear stress is very robust. While for the normal stress force F_z, the distribution is closer to a normal distribution, but not quite. In Fig. 6(b), we show a similar plot for the distribution of F_z. The semilog plot for the data from the two walls of the two different channels all fall on a single master curve that has an approximate parabolic shape but attempts to fit the data by a quadratic or a cubic function both fail. We found that at least a fourth degree fit is needed in order to describe the data. Further investigations reveal that the distribution of F_z actually follows quite close to the similarly standardized distribution of the local aperture of the channel, which is also added to Fig. 6(b) for comparison. For simulations of fluid flows in channels with different geometry, the probability distributions of F_z do not collapse but resemble the distributions of the aperture field of the respective channels.

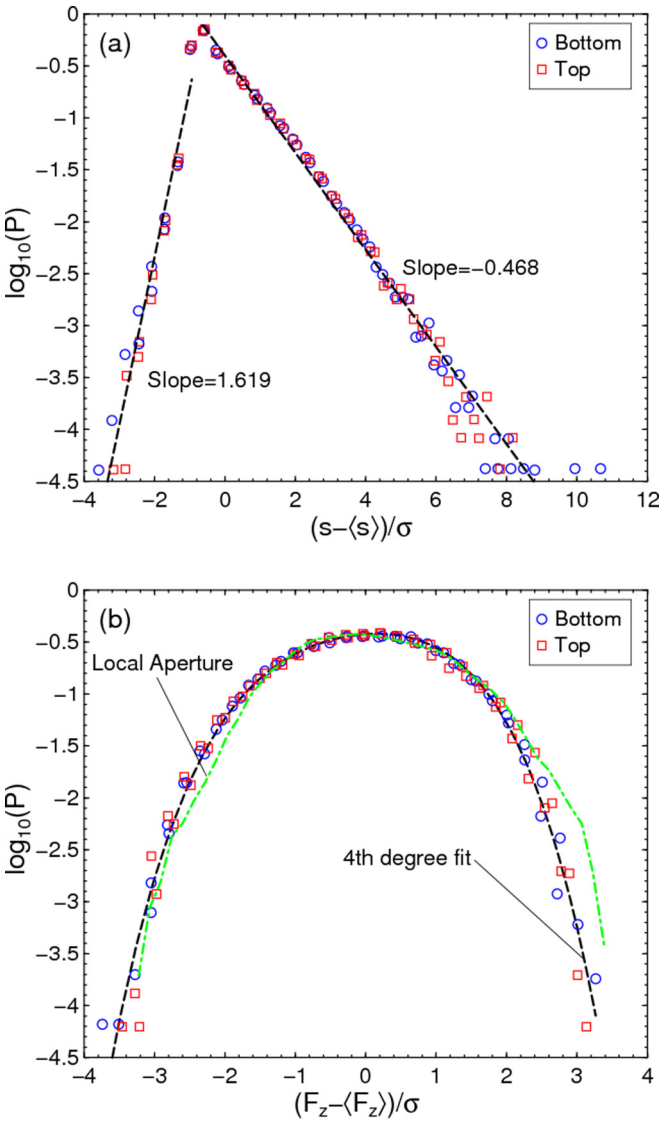

FIG. 6. (Color online) Probability distributions of (a) the local shear stress force and (b) the local normal force F_z acting on the two bounding surfaces for the pressure-driven flow of a pure fluid through the two channels in Fig. 2. Black dashed lines are fits to the data, and the green dash-dotted line in (b) is the distribution of the local aperture of the channel.

We have shown in Fig. 4 that spatial correlations in the aperture field would lead to nontrivial correlations in the velocity field for a fluid flowing through a fracture channel. It is natural to expect that similar correlations would also be manifested in the stresses. In Fig. 7, the spatial correlation functions, as defined in Eq. (1), for the shear stress force and the normal stress forces F_z and F_x are shown. Figure 7 includes data from the two bounding surfaces for the two different channels and are all plotted on the log-log scale. The normal stress force F_z in the z direction as shown in Fig. 7(a) clearly exhibits a power-law correlation over an extended range. But the exponent is about 1.03 which is much smaller than 1.6 as obtained from the Hurst exponent for the underlying surface. In the same plot, the correlation function for the shear stress force is also shown. Initially, the shear stress force shows similar

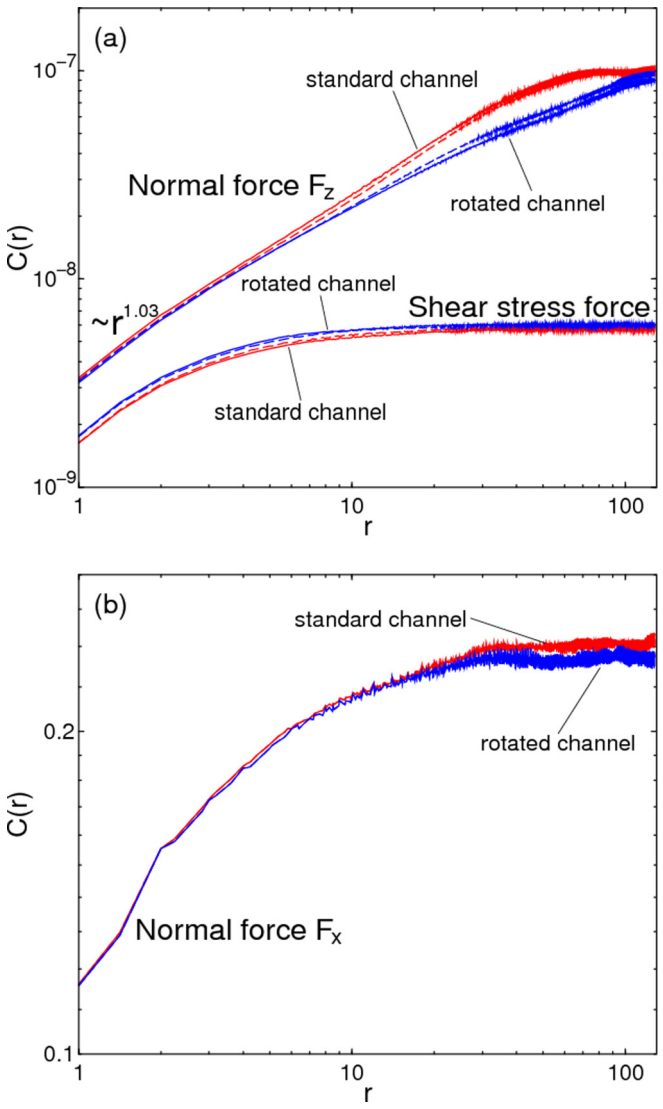

FIG. 7. (Color online) Spatial correlation functions of (a) the local shear stress force and local normal force F_z, and (b) the local normal force F_x in the x direction acting on the two bounding surfaces for the pressure-driven flow of a pure fluid through the two channels in Fig. 2. Solid lines are for the bottom surface and dashed lines are for the top. All axes are in log scale.

spatial correlations with roughly the same exponent, but the correlation is highly localized and decays very quickly when one moves away. On the other hand, the normal stress force F_x exhibits very little (almost no) correlation as indicated by the small differences on scale of the vertical axis in Fig. 7(b).

B. Simulations of flows with particles

In this section, we present the results for simulations of particulate flows in the model fracture channel as shown in Fig. 2. The main features of our work are that the mean aperture of the channel as well as the height fluctuations of the bounding surfaces are comparable to the size of the particles. The first feature defies treatment of effective medium approaches of any kind and mandates the necessity of tracking the dynamics of individual particles, while the second one requires a computation method that can handle random complex geometry effectively. The number of particles, N_p, in the simulations are 81, 163, 244, 325, and 407, which correspond to the bulk solid volume fraction ϕ in a range from 0.025 to 0.125. Three different realizations with different initial distributions of particles are used for each value of N_p. All particles and the fluid are set at rest at the start of the simulations and the calculations are run long enough to reach steady states.

We show in Fig. 8 the gap-averaged fluid and particle velocities in the steady states for the representative case of $N_p = 244$ particles flowing in the fracture channel as shown in Fig. 2(a). The density ratio for the simulations shown is $\rho_s/\rho = 1.06$ so gravity causes sedimentation effects in these cases. The corresponding runs for the neutrally buoyant case $\rho_s/\rho = 1.00$ where gravity has no effect are shown in Fig. 9. The value $N_p = 244$ is in the middle of the range of volume fractions considered here. The gap-averaged particle velocity field is defined in the same way as the gap-averaged fluid velocity before, except that only sites occupied by particles are included in the averaging in each column. Plots of the results of the same simulations for particles in the rotated channel in Fig. 2(b) are qualitatively similar. The first feature that we noted in these figures is that different initial particle configurations lead to distinctly different final states under the same flow conditions. In consequence, in this situation ensemble averaging is not at all equivalent to time averaging. In Figs. 8 and 9, the color scales indicate the magnitudes of the gap-averaged 2D velocities. The z components are ignored. The black color in the particle velocity maps are regions in the channels not occupied by any particle. Since each map is the time-averaged result in the steady state for a particular run, the continuous traces in the particle velocity maps indicate the trajectories of the traveling particles for that run and the localized (jammed) particles would form small circular patches on the maps. Note that periodic boundary conditions are applied to the mean flow (x) and the neutral (y) directions, so anything (particles and fluid) that leaves a boundary in the figures here would come in from the boundary on the opposite side. An interesting feature in the particle velocity maps is the existence of "hot spots," the few locations in the channel occupied by localized particles moving at very high average speed compared to other particles in the same run. The exact positions and speeds of the spots depend on the initial configurations that lead to different landscapes formed by the localized particles in the steady states. At this volume fraction $\phi = 7.5\%$, it seems that particles flow more readily in the neutrally buoyant case ($\rho_s/\rho = 1.00$), as indicated by the higher fraction of the channel filled up by the continuous paths in the particle velocity maps. The fluid velocity maps in Figs. 8 and 9 show that there is a kind of channeling effect within the fracture. It is obvious that the high fluid flow speed regions form elongated channels in the mean flow direction that roughly coincide with the particle flow paths or the particle-free regions. On the other hand, the low fluid speed dark regions are the area where localized particles deposited. So basically, depending on the random initial particle distributions, particles are moved by the flowing fluid until, at the steady state, different regions are jammed by deposited localized particles. These immobile

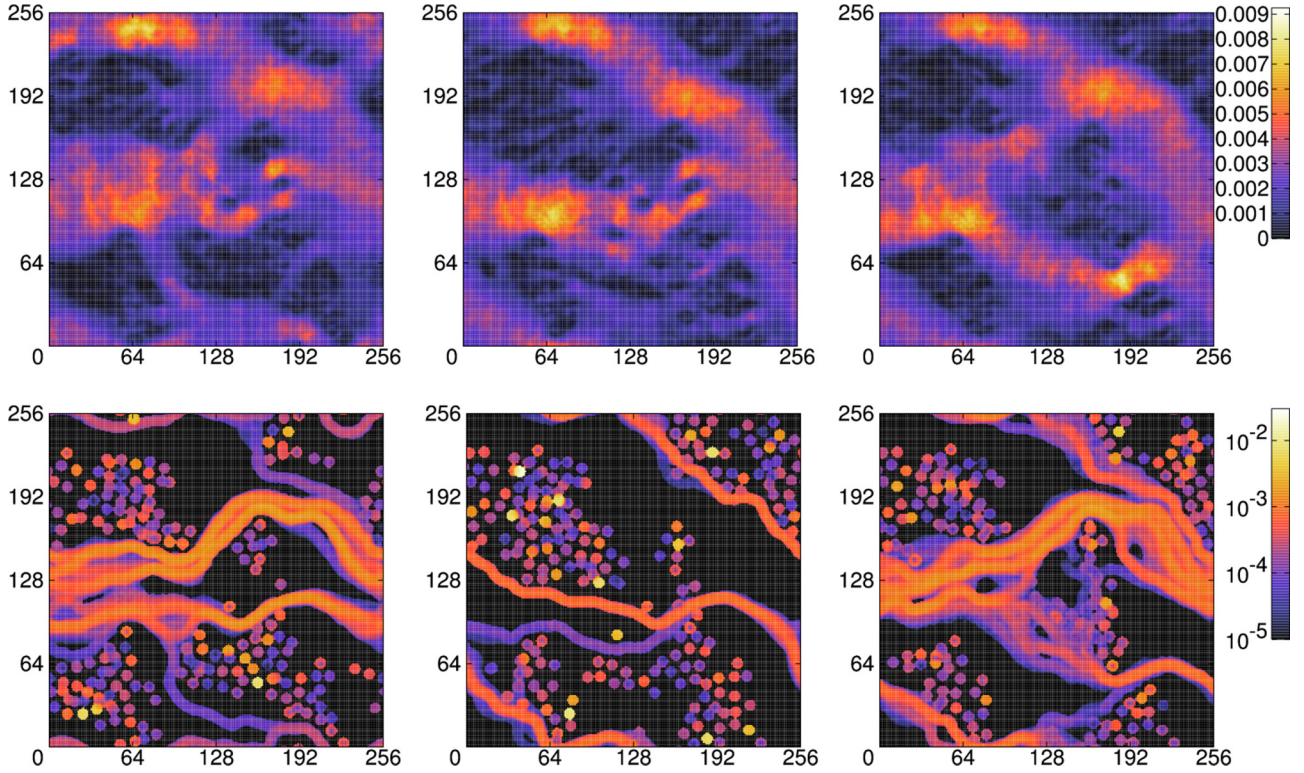

FIG. 8. (Color online) Steady-state gap-averaged 2D fluid (top row) and particle (bottom row) velocity fields for $N_p = 244$ ($\phi = 7.5\%$) and $\rho_s/\rho = 1.06$ for three different realizations for flows in the channel in Fig. 2(a).

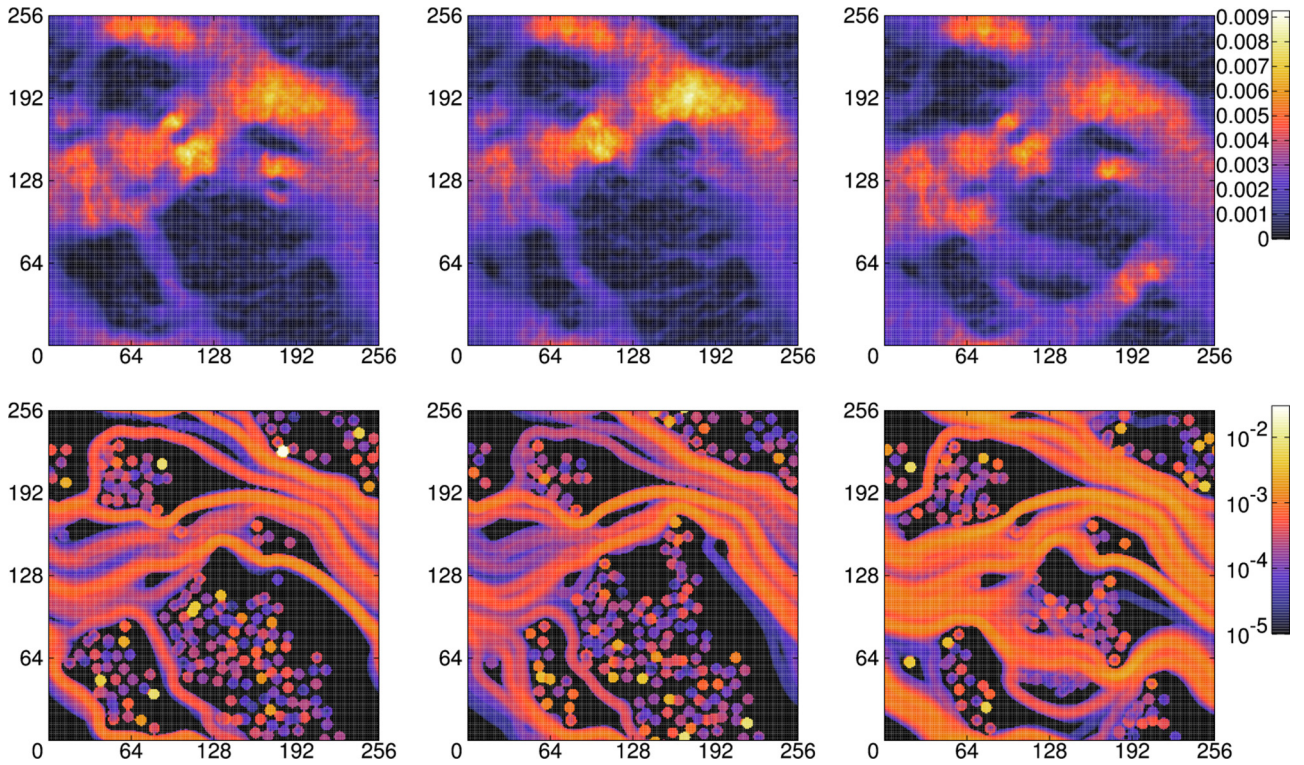

FIG. 9. (Color online) Steady-state gap-averaged 2D fluid (top row) and particle (bottom row) velocity fields for $N_p = 244$ ($\phi = 7.5\%$) and $\rho_s/\rho = 1.00$ for three different realizations for flows in the channel in Fig. 2(a).

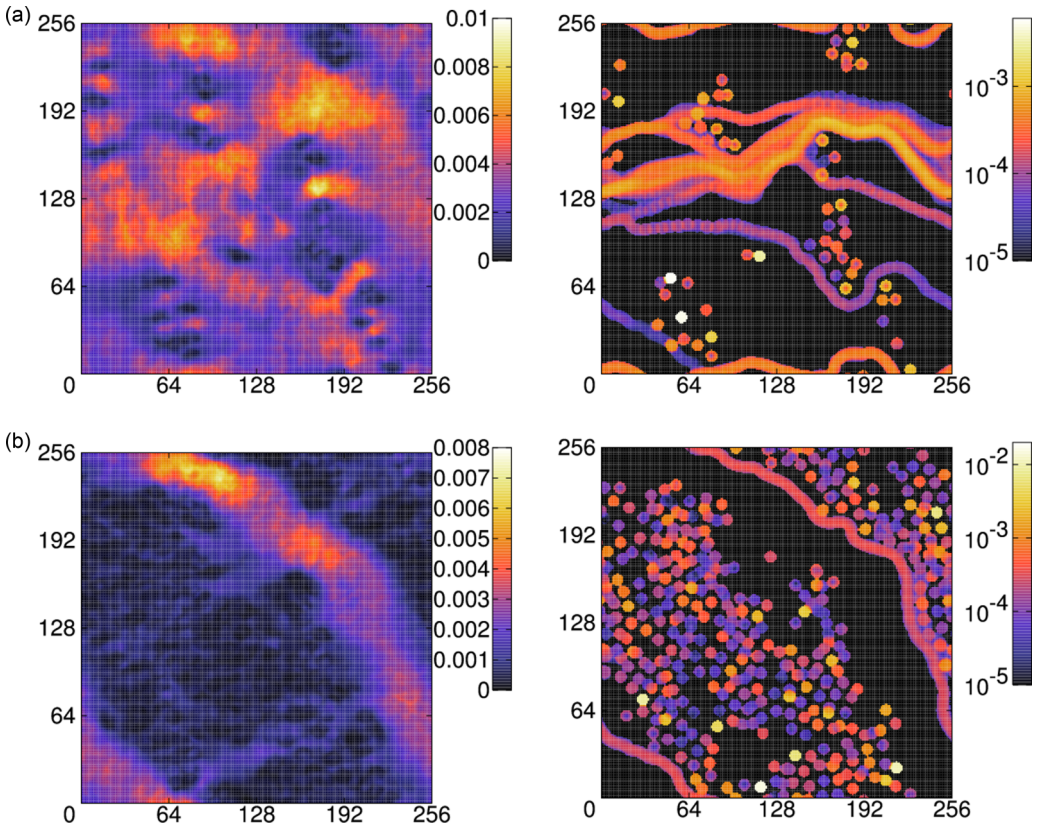

FIG. 10. (Color online) An example of steady-state gap-averaged 2D fluid (left) and particle (right) velocity fields for (a) $N_p = 81$ ($\phi = 2.5\%$) and (b) $N_p = 407$ ($\phi = 12.5\%$) particles flowing in the channel as shown in Fig. 2(a). The density ratio is $\rho_s/\rho = 1.06$.

particles together act as a static porous medium and modify the geometry of the fracture channel, and, depending on the final geometry, different flow patterns are formed.

In Fig. 10, examples of gap-averaged fluid and particle velocities for $N_p = 81$ ($\phi = 2.5\%$) and $N_p = 407$ ($\phi = 12.5\%$) are shown. The behavior of the systems is qualitatively similar to the case $N_p = 244$. Of course, at low volume fraction, the particle concentration is low enough that many particles are free to flow and only a few are trapped by the irregularities of the fracture. At high volume fraction, particles trapped by the fracture would block the motion of other particles, resulting in localization of a large fraction of solid particles. In fact, most of the particles in this example of $N_p = 407$ are trapped and the geometry of the fracture is modified so much that the "channel" for the fluid to flow is distorted. In some cases at high particle concentration, a complete jam may occur and no particle can flow.

Having discussed the flow patterns of particle suspension flows in fractures, we turn to the average behavior of the systems in more detail. In Fig. 11, the average fluid and particle velocities in the mean flow direction for all our simulation data are shown. Each symbol in these plots is the result of averaging over the whole channel and a time-averaging for frames in the steady state for each individual run with different initial particle configuration. The black dashed lines represent the average over three different realizations in each case. The data show that the average steady-state particle velocity depends on the initial conditions. As discussed, different initial particle configurations result in different steady states and we can see

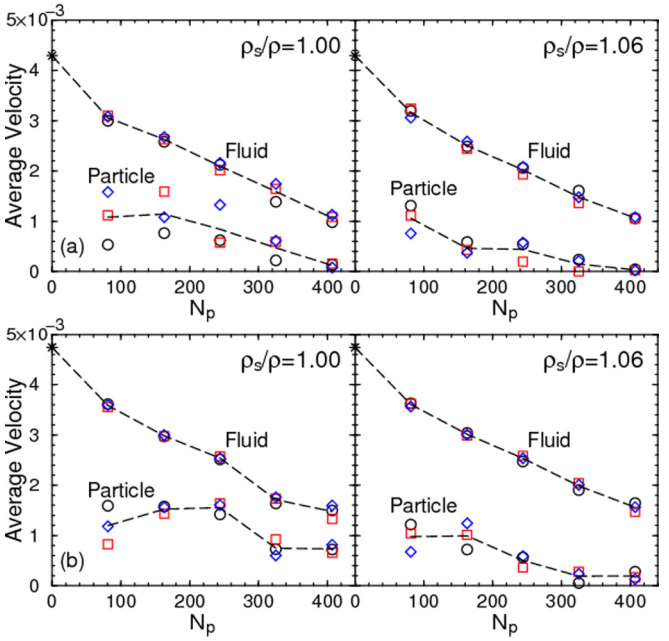

FIG. 11. (Color online) (a) Steady-state average fluid and particle velocities in the mean flow direction for flows in the channel shown in Fig. 2(a) at different particle concentrations for $\rho_s/\rho = 1.00$ and 1.06. (b) The same plots for the rotated channel in Fig. 2(b). Different symbols denote three different realizations and the dashed lines are the average over the three realizations. The stars represent the average fluid velocity for the pure fluid flow.

that the dispersion of the average particle velocities about the mean is large. On the other hand, the average steady-state fluid velocity is not sensitive to the initial particle configuration, as indicated by their small dispersions about the mean. As the number of particles N_p in the channel increases, both the average fluid and particle velocities tend to decrease as expected because increasing N_p would result in more particles being trapped, which would reduce the free space volume of the channel and increase the resistance to the flow. In a bulk unconfined homogeneous particulate suspension, one would usually explain the reduction in the flow rate as the particle concentration increases in terms of the effective viscosity of the suspension. But here we have an inhomogeneous confined system with complex boundary geometry, the usual concept of effective viscosity cannot be applied. For example, particle trapping by irregular walls is completely absent in a bulk homogeneous suspension, and no space in our channel is in the "bulk." When comparing the results for $\rho_s/\rho = 1.00$ to those for $\rho_s/\rho = 1.06$, we find that the difference in density ratio does not make a significant difference, as opposed to the case of open fractures [18]. The average fluid velocities are almost identical for the two density ratios. The average particle velocities for the two density ratios are also quantitatively similar. The only small difference is in the particle velocities at large N_p where the average velocity is lower for the higher density ratio, indicating that the particles are more immobile. One explanation for the insensitivity to the density ratio is the small mean aperture compared to the particle size. Because the width of the channel is so narrow and the height fluctuations in the walls are comparable to the particle size, the particles are blocked by the irregularities of the walls anyway. The high density ratio causes sedimentation and results in particles settling down at the bottom of the channel in the steady state. Since the trapped particles almost always fill up the gap between the two walls no matter whether they sink to the bottom or not, there is not much difference in the landscape created by the trapped particles. So basically the fluid sees a similar effective geometry in either case; therefore, the average fluid velocity is almost the same in both cases.

Next we turn our attention to the average shear stress acting on the two walls of the fracture channel. This is a quantity of practical interest since the mechanical response of the solid depends on the forces acting on it. Similarly to Fig. 11, the steady-state shear stresses averaged over the entire wall for all our simulations are presented in Fig. 12. As in Fig. 11, the symbols denote different realizations and the black dashed line is the average over three different realizations for each N_p. Figure 12 shows that the average shear stress decreases as N_p (or ϕ) increases, presumably due to the reduced flow rates. The ranges in the stress in Fig. 12(a) and Fig. 12(b), which represent flows in two different orientations, slightly differ. When comparing results for the two different density ratios, we see that the average shear stresses are also quantitatively similar. However, the density ratio definitely makes a difference between the upper and the lower walls. At $\rho_s/\rho = 1.00$ the particles are neutrally buoyant and the top and bottom walls are the same, and, as a result, the shear stresses acting on the two walls are almost identical. On the other hand, sedimentation causes the particles to accumulate near

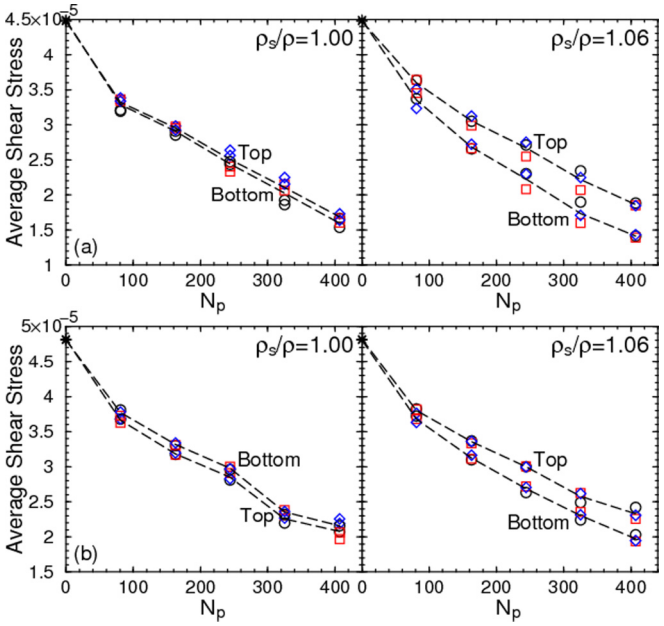

FIG. 12. (Color online) (a) Steady-state average shear stress acting on the two surfaces of the fracture for flows in the channel shown in Fig. 2(a) at different particle concentrations for $\rho_s/\rho = 1.00$ and 1.06. (b) The same plots for the rotated channel in Fig. 2(b). Different symbols denote three different realizations and the dashed lines are the average over the three realizations. The stars represent the average shear stress for the pure fluid case.

the bottom surface and makes them harder to escape from the irregularities at a higher density ratio $\rho_s/\rho = 1.06$. As particles are trapped and immobilized, they increase the resistance to the flow and reduce the fluid speed near the bottom wall. At the same time, the layer near the top wall should be relatively free of particles so the thin fluid layer near the upper surface should flow a little faster. So one would expect the shear stress at the top wall should be higher than the stress at the bottom, and that is the case seen in Fig. 12. Though the intuition of this way of thinking is based on the picture of a wide open channel and it may not be completely correct in the case of narrow fracture here, results in Fig. 12 suggest that this picture should still be roughly correct.

Now we turn to the steady-state average normal force F_x acting in the mean flow direction in Fig. 13. This component is the force acting on a vertical section of the wall in the flow direction due to the fluid flowing in the same direction and would vanish for a flat channel. At each point, this component actually contains a hydrostatic pressure part as well as a viscous contribution σ_{xx}, but since the walls have both forward- and backward-facing parts, the hydrostatic pressure tends to cancel out when averaging over the whole wall, so at the end, F_x represents a net "drag" force acting on the wall in the mean flow direction. Same as before, the symbols denote results of individual runs and dashed lines represent averaging over different realizations at each N_p in Fig. 13. From the figure, we see that F_x decreases as the particle concentration increases, which can be related to the reduced flow rate at high particle concentration. However, besides the particle concentration, the flow rate as well as the flow pattern also depend on

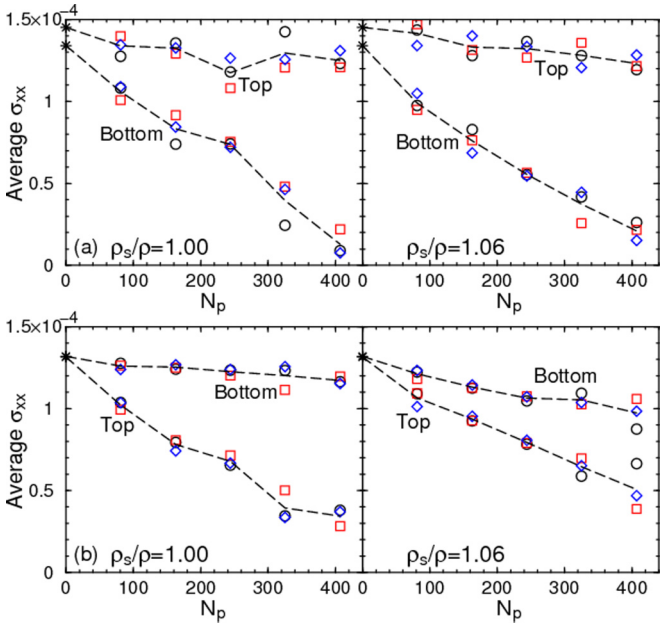

FIG. 13. (Color online) (a) Steady-state average normal force F_x acting on the two surfaces of the fracture for flows in the channel shown in Fig. 2(a) at different particle concentrations for $\rho_s/\rho = 1.00$ and 1.06. (b) The same plots for the rotated channel in Fig. 2(b). Different symbols denote three different realizations and the dashed lines are the average over the three realizations. The stars represent the average normal force F_x for the pure fluid case.

other variables such as the geometry of the bounding walls, the orientation of the channel with respect to the flow, and the final distribution of the jammed particles that essentially varies from one realization to another, and the dependence on these complicated factors is not well understood. When comparing the results for the neutrally buoyant cases to the corresponding results at $\rho_s/\rho = 1.06$ in Fig. 13, we find that the results are similar. When we examine the final distributions of the jammed particles for each realization for the two density ratios at the same N_p, we also find that the configurations are similar, though differences in details exist (for example, see Figs. 8 and 9). On the other hand, when results for flows in different orientations are compared [Fig. 13(a) and 13(b)], the results differ substantially. In particular, even the magnitudes of the averaged force acting at the top and bottom surfaces are switched. We do not understand the exact causes that make the difference at the moment, but it may be due to the differences in the geometry and the final configurations of the jammed particles in the two cases because σ_{xx} acting on the walls depends sensitively to the details of the flow field next to the walls, which in turns depends on the geometry of the surfaces and the final distributions of the jammed particles.

Finally, we analyzed the distributions of the shear stress force and the normal force F_z acting on the bounding walls of the two fracture channels in Fig. 2 for pressure-driven particulate suspension flows in the steady state. Following Fig. 6, we show in Fig. 14 the logarithm of the probability distributions of the shear stress and the normal force F_z for $N_p = 0$ (pure fluid), 81, 244, and 407. Data for the other two volume fractions are not shown here for clarity. The shear stress and the normal force on the x axes of the figures are

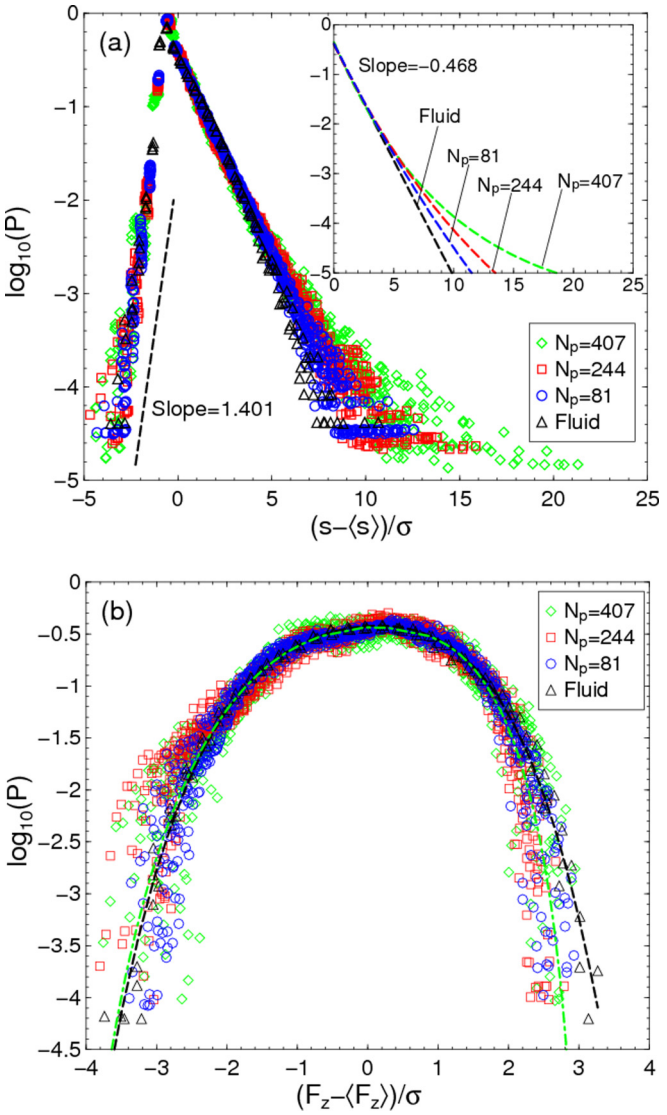

FIG. 14. (Color online) Probability distributions of (a) the local shear stress force and (b) the local normal force F_z acting on the two bounding surfaces for particulate suspension flows at different nominal particle concentrations through the two channels in Fig. 2. Inset of the figure in (a) are smooth fits to the raw data for the distribution above the maximum. Black dashed and green dash-dotted lines in (b) are smooth fits to the pure fluid data and all the data sets shown combined, respectively.

standardized in the same way as in Fig. 6. For each value of N_p, the data set includes results from all realizations and flows in two orientations at the two density ratios, as well as the forces acting on both the upper and the lower walls. For each individual run, the mean and the standard deviation vary and differ, even for the two walls. But after the standardization, the distributions are very robust. First, let us focus on the shear stress distribution in Fig. 14(a). The figure shows that the distribution of the shear stress collapse into two groups for stresses above and below a maximum close to the mean. Each group roughly follows an exponential distribution with its own decay rate. The decay rates (i.e., slopes of the straight lines) are similar to those for pure fluid flows in Fig. 6. For stresses below the maximum, all data sets collapse almost to

a single straight line with very little dispersion. On the other hand, data for all values of N_p for stresses above the maximum collapse to a single straight line only for low stresses within five standard deviations from the mean. At higher shear stress, the distributions start to differ and the dispersion is large for larger N_p. We believe that the large variations at higher particle concentrations are due to different final configurations of the jammed particles in different realizations. Note also that even though the trapped particles in the final configurations are localized in the global sense, they are always jiggling around vigorously locally and this would create more variations in the local stress. Usually, a Gaussian probability distribution is an indication of a sum of independent random events. The fact that the shear stress distributions here are exponential instead of Gaussian indicates that the local shear stress at different parts of the walls are correlated somehow.

Now we turn the the normal force distribution in Fig. 14(b). The black dashed line and the fluid data set are the same ones as in Fig. 6. Data at various values of N_p are denoted by different symbols and the green dashed line is a smooth fit of all data sets combined. We can say that the data all collapse roughly to a single distribution similar to the one for pure fluid. For small force F_z within roughly two standard deviations from the mean, the dispersion in the data from the fit is small. For data below the mean, the averaged distribution (green dashed line) is actually almost identical with the fluid data (black dashed line). But for F_z above the mean, there is some differences between the fluid and the data sets with particles. The normal force distribution for pure fluid flows is more symmetric. In any case, the distribution is definitely not Gaussian. In the case of pure fluid flows, we show in Fig. 6 that the distribution of F_z roughly follows the one for the aperture field. With particles, the localized trapped particles in the steady state would modify the channel geometry and the distributions of the trapped particles differs for different realizations. This fact at least partly explains the dispersions for data sets with $N_p \neq 0$.

IV. CONCLUSIONS

In this work, we have used numerical simulations to investigate pressure-driven flows of particulate suspensions of spherical solid particles in a Newtonian fluid in a narrow fracture channel formed by two complimentary self-affine solid walls that are separated by a displacement normal to the mean plane and shifted relative to each other by a shear displacement. Transport of the same material flowing in open fractures and channels with flat walls were studied in previous papers [17,18]. The case of a pure fluid flowing through such a channel without particles is also studied for comparison. The spatial correlation function of the height profile of a self-affine surface assumes the form of a power law characterized by the Hurst exponent H [see Eq. (1)]. As a result, the aperture field of the channel is also spatially correlated and has the same power-law correlation in a range up to the size of the shear displacement. The geometry of the channel used in this study is as close to a realistic geological fracture as possible and our work here is the most realistic in this sense in studies of this kind. The size of the particles is comparable to both the mean aperture of the channel and the fluctuation in the height of the bounding surfaces. Our emphases here is the interplay between the confinement effect due to narrow channel width and the blockage of particle motion due to irregularities in the walls. As opposed to the case of open fractures in Ref. [18], resuspension effects do not play a role here because the wall irregularities have the same length scale as the channel aperture.

In the absence of particles, the flow rate for a fluid flowing through a fracture channel is highly reduced relative to an equivalent channel with flat walls of width equal to the mean aperture of the channel, and obviously the precise rate depends on the geometry of the specific channel and the orientation of the flow. Due to perturbations by the irregular walls, the local flow field is spatially nonuniform. However, fast flow regions tend to form elongated channels in the direction of the pressure drop irrespective of the orientation of the channel. The fluid velocity field for flows in a fracture channel is spatially correlated in a range similar to the correlation length of the aperture field and the correlation functions have the form of a power law. We find that the two velocity components v_y (neutral direction) and v_z (vertical direction) have the same exponent in their correlation functions, but for v_x (mean flow direction) the exponent in the correlation function is smaller.

In connection with the mechanical responses of the walls of the fracture, we analyzed the forces exerted on the two bounding surfaces when a fluid flowing through the channel. The local normal force F_z in the vertical direction is dominated by the hydrostatic pressure with small fluctuations, and it is spatially correlated with a power-law correlation in an extended range similar to that of the bounding surfaces. However, the exponent is less than H. The probability distribution of F_z acting on the two walls are the same and follows the distribution of the aperture field when suitably normalized. The local shear stress force acting on the two bounding surfaces is also spatially correlated, but only in a range similar to the shear displacement, which is much smaller than the correlation length for F_z. However, the probability distribution of the shear stress, when normalized, has a universal exponential form which is very robust. Another interesting feature is that even though the total shear stress forces acting on the two walls are positive (i.e., in the mean flow direction), the local shear stress has large fluctuations and can be negative locally. The local normal force F_x is the force acting on a wall in the x direction (the mean flow direction) due to the fluid flowing in the same direction. This force would vanish for a flat channel and is a new feature for rough fracture walls. The magnitude of this component is also dominated by the hydrostatic pressure with local fluctuations due to heterogeneities in the flow field. The distribution of the local force F_x has large fluctuations that depend on the local orientation and area of the vertical protrusion of the irregular walls and the local force can be positive or negative. However, its average over the entire wall is positive, consistent with the flow in the positive x direction. In contrast with F_z and the shear stress force, the normal force F_x shows very little spatial correlation.

For particle-laden flows the situation is more complicated because the particles may become trapped and then act as a filter or static porous medium and modify the geometry of the channel. Furthermore, the structure of the final steady state depends on the initial configuration of the particles, which dictates which regions of the channel become jammed

by trapped particles. The opposite behavior is found in the suspension flows in open fractures, studied in Ref. [18], where most of the steady-state results are independent of the initial particle distribution (unless the overall particle concentration is so high as to suppress relative particle motion). Ensemble averaging is appropriate to identify mean behavior in the latter case but not here, where different realizations may have distinctly different behavior.

One result of particle jamming in the fracture is the channeling effect observed for pure fluid flows that now occurs for both fluid and particles, although the detailed flow fields differ. Regions of the fracture where particles deposit have an altered geometry where fluid velocities are reduced, which promotes flow elsewhere. The preferential fluid channels thus vary with deposition and, in turn, on the concentration and initial distributions of the particles. Similarly, the preferred particle channels do not simply coincide with regions of fastest fluid flow but require a local aperture greater than the particle diameter, in addition to the fact that their presence and deposition affect the flow field of the carrying fluid. These interdependent complications produce distinct spatial distributions of rapid fluid and particle motion, although we do observe some overlap of the two. The heterogeneity of particle deposition, in tandem with the random geometry of the fracture, leads to a local flow which may deviate significantly from the direction of the pressure drop [for example, see Fig. 10(b)].

As for the global flow rates, both the average fluid and particle velocities (in the mean flow direction) decrease as the particle concentration increases since high particle concentration leads to more particle jamming and produces more resistance to fluid flow. The fluid flux is insensitive to the final particle distribution, whereas the average particle velocity changes from one realization to another. Gravity does not have a significant effect on the global flow rates in these tight narrow fractures. The average shear stress acting on the bounding walls of the fracture also decreases as the particle concentration increases, due to the reduced fluid velocity. In contrast with the global flow rates, gravity does play a role in determining the stresses because sedimentation and trapping of particles near the bottom wall reduces fluid flow in that region and creates a thin layer of faster flowing fluid near the top. For neutrally buoyant particles, the top and the bottom are statistically the same as is the stress. But for denser particles, the shear stress on the top wall is larger than the stress on the bottom (see Fig. 12). Even though the channel geometry is considerably modified by trapped particles, the distributions of the local shear stress on the walls are remarkably similar to the one for pure fluid (Fig. 14), aside from stronger fluctuations at high stress. The stress distribution is exponential and very robust over a wide range. As with the local shear stress, the distributions of the local normal force F_z acting in the vertical direction are also very similar to the one for pure fluid except for more fluctuation in the case with particles, probably due to a variety of final distributions of trapped particles in the steady state. Finally, for the average "drag" force, i.e., the normal force F_x in the x direction due to fluid flowing in the same direction averaged over the whole wall, the general trend is a decrease as particle concentration increases because average flow rates decrease.

Ultimately, our goal is to relate the transport of fluid and particles to the fracture geometry, at least in a statistical manner, a difficult problem due to the interactions among the fluid, the particles, and the random wall geometry. The three relevant length scales are the particle size, the mean aperture of the channel, and the roughness of the bounding walls. For a narrow, geologically realistic fracture, the problem is exacerbated because all three length scales are comparable, which makes analyses based on continuum or perturbation approaches unsuitable and requires tracking of the dynamics at the particle level. Although many of the results and trends observed in the simulations are qualitatively consistent with simple physical intuition, new and surprising results arise, such as the exponential distribution of the shear stress acting on the bounding walls and the nontrivial distribution of the normal force. The origin of these distributions is not understood at present. We further observed power-law correlations in the velocity field and in the normal force and shear stress acting on the walls for fluid flowing through a fracture. The existence of such spatial correlations might be anticipated as a consequence of the correlations in the bounding surfaces where the no-slip boundary conditions are applied. However, the exponents observed in the correlation functions in general differ from the underlying Hurst exponent, and further analysis will be required to obtain the connections between them.

ACKNOWLEDGMENTS

This work was supported by the Geosciences Program of the US Department of Energy, with computational resources provided by NERSC.

[1] P. M. Adler and J.-F. Thovert, *Fractures and Fracture Networks* (Kluwer, Dordrecht, 1999).
[2] J. Bear, C. F. Tsang, and G. de Marsily, *Flow and Contaminated Transport in Fractured Rock* (Academic Press, San Diego, CA, 1993).
[3] M. Sahimi, *Flow and Transport in Porous Media and Fractured Rock* (VCH, Weinheim, 1995).
[4] B. Berkowitz, Adv. Water Resour. **25**, 861 (2002).
[5] J. Feder, *Fractals* (Springer, New York, 1988).
[6] E. Bouchaud, J. Phys.: Condens. Matter **9**, 4319 (1997).
[7] P. A. Witherspoon, J. S. Y. Wang, K. Iwai, and J. E. Gale, Water Resour. Res. **16**, 1016 (1980).
[8] C.-F. Tsang and I. Neretnieks, Rev. Geophys. **36**, 275 (1998).
[9] S. Sirivithayapakorn and A. Keller, Water Resour. Res. **39**, 1109 (2003).
[10] C. Chen, B. L. T. Lau, J.-F. Gaillard, and A. I. Packman, Water Resour. Res. **45**, W06416 (2009).
[11] S. A. Bradford, S. Torkzaban, F. Leij, J. Šimůnek, and M. T. van Genuchten, Water Resour. Res. **45**, W02414 (2009).

[12] S. Succi, *The Lattice Boltzmann Equation for Fluid Dynamics and Beyond* (Clarendon Press, Oxford, 2001).
[13] G. Drazer and J. Koplik, Phys. Rev. E **66**, 026303 (2002).
[14] G. Drazer, H. Auradou, J. Koplik, and J. P. Hulin, Phys. Rev. Lett. **92**, 014501 (2004).
[15] H. Auradou, G. Drazer, J.-P. Hulin, and J. Koplik, Water Resour. Res. **41**, W09423 (2005).
[16] Y. Yan and J. Koplik, Phys. Rev. E **77**, 036315 (2008).
[17] Y. Yan and J. Koplik, Phys. Fluids **21**, 013301 (2009).
[18] T. S. Lo and J. Koplik, Phys. Fluids **24**, 053303 (2012).
[19] A. J. C. Ladd, J. Fluid Mech. **271**, 285 (1994).
[20] E. J. Ding and C. Aidun, J. Stat. Phys. **112**, 685 (2003).
[21] N.-Q. Nguyen and A. J. C. Ladd, Phys. Rev. E **66**, 046708 (2002).
[22] R. Verberg and D. L. Koch, Phys. Fluids **18**, 083303 (2006).
[23] Y. Yan, J. F. Morris, and J. Koplik, Phys. Fluids **19**, 113305 (2007).
[24] R. F. Voss, *Fundamental Algorithms in Computer Graphics* (Springer-Verlag, Berlin, 1985), pp. 805–835.
[25] F. Plouraboué *et al*., Phys. Rev. E **51**, 1675 (1995).
[26] T. Krüger, F. Varnik, and D. Raabe, Phys. Rev. E **79**, 046704 (2009).